



PII S0016-7037(97)00165-8

Differential redox and sorption of Cr(III/VI) on natural silicate and oxide minerals: EXAFS and XANES results

MARIA L. PETERSON,^{1,*} GORDON E. BROWN, JR.,^{1,2} GEORGE A. PARKS,¹ and CAROL L. STEIN³¹Department of Geological and Environmental Sciences, Stanford University, Stanford, California 94305-2115, USA²Stanford Synchrotron Radiation Laboratory, Stanford, California 94309, USA³School of Oceanography, University of Washington, Seattle, Washington 98195, USA

(Received September 1, 1996; accepted in revised form April 18, 1997)

Abstract—Synchrotron-based X-ray absorption fine structure (XAFS) spectroscopy was used to investigate the reduction of aqueous Cr(VI) to Cr(III) in magnetite-bearing soils from Cr-contaminated sites. Soils from two field sites were examined, showing that mixed-valence Cr(III/VI) effluent is reduced to Cr(III) when associated with the magnetite fraction of the soil, whereas the Cr effluent associated with non-Fe(II)-bearing minerals results in mixed Cr(III/VI) adsorbates or precipitated phases. The Fe²⁺ in magnetite, Fe²⁺Fe₂³⁺O₄, may act as an electron source for heterogeneous Cr(VI)-to-Cr(III) reduction, converting magnetite topotactically to maghemite, γ-Fe₂³⁺O₃. The ratio of Cr(VI)/total Cr was determined by the height of the Cr(VI) XAFS pre-edge feature, which is due to a 1s to 3d electronic transition. This pre-edge feature was calibrated as a function of Cr(VI)/Cr(III) using mixtures of Cr(III) and Cr(VI) model compounds. Environmental remediation of Cr-contaminated sites requires knowledge of chromium oxidation and speciation, and XAFS spectroscopy may be used to supply both types of information with minimal sample processing or data analysis. Copyright © 1997 Elsevier Science Ltd

1. INTRODUCTION

Cost-effective and efficient environmental remediation of sites contaminated by Cr requires knowledge of the chromium oxidation states present, i.e., Cr(III), Cr(VI), or both, and the mode(s) of Cr sorption to or precipitation on the minerals present in the affected soil. Over the pH range of most natural ground waters, trivalent Cr is thermodynamically more stable as a sorbed surface complex or in a solid phase, such as an oxyhydroxide precipitate, than as an aqueous complex. The environmental hazard posed by trivalent Cr, therefore, tends to be localized to the region where it has sorbed or precipitated. Hexavalent Cr species, however, are thermodynamically stable as anionic solution species, in the absence of a reductant such as Fe(II), over the same range of pH where Cr(III) species tend to precipitate, making Cr(VI) the more mobile and, potentially, the more bioavailable of the two dominant oxidation states.

Chromium is essential to human health, as it is important for glucose metabolism. The maximum recommended intake of Cr for humans is 0.05 mg L⁻¹ (Public Health Service, 1962). Above this threshold, ingested Cr may have serious health consequences including tumors, ulcers, and cancer induced by alteration of the DNA template (Snow and Xu, 1989; Lewis, 1991). In addition, the more oxidized and mobile form, Cr(VI), has been found to be more toxic than Cr(III) to various microbiota (Babich and Stotzky, 1983).

Immobilization of aqueous Cr species is a first step in the localization of regions of Cr-contamination, but further remediation steps must rely on knowledge of what solids or sorbed phases are present as well as their mode(s) of sorption or precipitation. The modes of sorption or precipitation

of Cr(III) and Cr(VI) are quite different, reflecting their different aqueous ionic states (cationic vs. anionic), oxidation state (+3 vs. +6), valence band structure (d³ vs. d⁰), and local coordination geometry (octahedral Cr(III)O₆ vs. tetrahedral Cr(VI)O₄). Knowledge of the relative proportions of Cr(III) and Cr(VI) present, therefore, plays a major role in the selection of an appropriate remediation strategy for Cr-contaminated sites.

The rate of Cr(VI)-to-Cr(III) reduction is highly dependent on numerous factors: the local ground water and mineral chemistry prior to the contamination event or prior to the installation of the chemical waste disposal facility; the solid and solution compositions of the waste or effluent; and chemical changes over time as reactions occur. Much of this information is commonly unavailable for Cr-contaminated sites. Reduction of Cr(VI) to Cr(III) in laboratory experiments with 0.01–2 mM Cr and at near-neutral pH occurs on the order of <1–10 min for reaction with aqueous ferrous ion (Eary and Rai, 1988; Fendorf and Guangchao, 1996), within 8–10 h for reaction with synthetic magnetite (Peterson et al., 1996a), and for reactions with natural soils, rapid reduction occurs for 24–48 h followed by slower reduction rates for up to 6 weeks (Eary and Rai, 1991). Based on this range of Cr(VI) reduction rates, we assume that the Cr(VI):Cr(III) ratios have reached steady-state values at the two field sites examined in this paper: a Cr plating facility near Keyport, WA and a chemical waste disposal site at Sandia National Laboratory, Albuquerque, NM. At each site, the introduction of Cr into the environment occurred several years prior to our chemical examination of the affected soils.

The goals of this research were (1) to determine the Cr(VI)/total Cr ratio of Cr-contaminated soils from two field areas; (2) to determine the Cr species present and their mode(s) of sorption to or precipitation on soil minerals; and

* Present address: EKC Technology, Inc., 2520 Barrington Court, Hayward, California 94545-1163, USA.



(3) to test the hypothesis that Cr(VI) is reduced to Cr(III) by reaction with the Fe^{2+} -bearing mineral magnetite at Cr-contaminated field sites, as has previously been observed in laboratory studies (Peterson et al., 1996a; White and Peterson, 1996). Such Cr(VI)-to-Cr(III) reduction has also been observed at the surface of other Fe minerals such as Fe^{2+} -bearing FeOOH (Bidoglio et al., 1993) and biotite (Ilton and Veblen, 1994), and has been reported to occur in situ in Cr-contaminated soils containing ferrous minerals (Anderson et al., 1992; Kent et al., 1994). X-ray absorption fine structure (XAFS) spectroscopy was used in this study to quantify Cr(VI)/total Cr content and to identify Cr species associated with Cr-contaminated soil minerals, and precipitate phase identification was verified by electron microprobe analysis.

2. MATERIALS

2.1. Chromium-Contaminated Soils

Soil samples were collected from two sites: a Cr plating facility near Keyport, WA, USA, where a corroded disposal pipe allowed seepage of Cr effluent into the surrounding soil, and a chemical waste landfill containing several surface disposal pits for chromium and other chemical waste solutions, in use from the 1960s until the early 1980s, at Sandia National Laboratory, Albuquerque, NM, USA. The moisture content of the soils was between 5 and 15%. Soils were dried and stored under ambient conditions for subsequent analysis. The soil mineralogy of both sites is dominated by silicate minerals, primarily quartz and plagioclase feldspar, as determined by X-ray diffraction (XRD), with accessory magnetite present in most samples. In order to observe possible Cr(VI) reduction on the Fe^{2+} -bearing magnetites, the magnetic fraction was separated from the bulk soil of both Keyport and Sandia samples by use of a hand-held magnet encased in a latex sheath (a glove finger), a method that allows easy separation of the magnetite from the magnet. The mineral separates were powdered using a mortar and pestle prior to XAFS analysis.

2.2. Chromium Model Compounds

Chromium(III) compounds used for XAFS modeling and pre-edge height calibration included chromite (FeCr_2O_4) from Black Lake, Megantic County, Quebec, Canada and synthetic Cr_2O_3 , 99.995% purity. The Cr(VI) model compounds were $\text{Na}_2\text{CrO}_4 \cdot 4\text{H}_2\text{O}$ and CaCrO_4 , analytical reagents. Physical mixtures of Cr_2O_3 and $\text{Na}_2\text{CrO}_4 \cdot 4\text{H}_2\text{O}$ in molar ratios containing 0, 20, 40, 60, 80, and 100% Cr(VI)/total Cr were used for calibration of the XAFS pre-edge feature. The degree of hydration of these compounds was determined by drying known amounts of the compounds at 190°C overnight and comparing the weights before and after drying. The Cr_2O_3 was determined to have less than 0.03 wt% water, and the $\text{Na}_2\text{CrO}_4 \cdot 4\text{H}_2\text{O}$ had 4.006 waters of hydration. Bulk phase identification of each model compound was verified by XRD.

3. INSTRUMENTAL ANALYSIS

3.1. Chromium Content Analysis

Total Cr in the soil samples was determined by sample digestion or sequential extraction, followed by analysis of the solution Cr content (method discussed in Tessier et al., 1979). The digestion method used 300 mg soil samples placed in 23 mL Parr bombs with 2 mL of concentrated HNO_3 and 10 mL of concentrated HF. The bombs were placed in an oven for 12 h at 130°C. The capsules were evaporated to dryness and the residue redissolved in 1% HNO_3 . Solutions were subsequently analyzed for Cr content

by direct current plasma emission spectrometry (DCP) or inductively coupled plasma spectrometry (ICP).

3.2. X-Ray Photoelectron Spectroscopy

X-ray photoelectron spectroscopy (XPS) was performed using a Surface Science Instruments S-Probe system with monochromatic Al $K\alpha$ radiation (1486.7 eV). A charge neutralization gun set at 0.5 V and a Ni screen placed approximately 1 mm above the sample surface were used to reduce charging effects (Briggs and Seah, 1990). Depth profiling analyses were performed by Ar beam sputtering. Survey and region scans were collected before sputtering and after each sputtering interval. The survey spectra were collected from 1 to 1000 eV with a $250 \mu\text{m} \times 1000 \mu\text{m}$ spot size, 1 s per data point, and step size 1 eV to determine the elements present. Five scans were averaged for each of the survey spectra. Region scans over the Cr2p and Fe2p peaks (for the magnetic mineral fractions) or Cr2p and Si2p (for the silicate mineral fractions) were collected over a 30 eV scan range encompassing the peak, with pass energy 50 eV, 1 s per data point, and step size 0.06 eV. In order to improve signal quality, ten scans were averaged for each Fe2p and Si2p peak measurement and forty scans were averaged for each Cr2p peak measurement. The sputter rate of Ar ion bombardment to remove surface layers was calibrated by sputtering a 300 Å carbon coating on brass until the brass color was visible. A sputter rate of 16–18 Å min^{-1} of carbon removed over a 2 mm \times 2 mm beam raster area was calculated. To calculate the sputter rate of Cr surface coatings, we assumed that Cr surface coatings are removed at the same rate as other oxides such as SiO_2 , which sputters at a rate ≈ 6 times that of C, or Cr in stainless steel, which sputters at a rate ≈ 5 times that of C. Thus the removal rate of Cr sputtered from the mineral surfaces was calculated to be approximately $100 \pm 20 \text{ Å min}^{-1}$.

3.3. Electron Microprobe Analysis

Mineral grains from each of the soil samples were mounted in epoxy on glass slides, polished, carbon coated, and analyzed by backscattered electron spectroscopy (BES) and Cr X-ray analysis on a Jeol Superprobe 733, operated at 15 keV. To get a large quantity of grains in a small area for BES analysis, 1 cm diameter, 2 mm high glass rings were affixed to glass slides to make an enclosure for the mineral grains which were then set with epoxy and polished. The Cr content present in the bulk of the magnetites was measured by quantitative microprobe analyses on multiple points in the interiors of twelve individual grains of the Keyport magnetic mineral separate. This measurement was done to determine if naturally occurring Cr in the magnetite structure might contribute significantly to the XAFS signal arising from surface-associated Cr which may be present due to the Cr effluent contamination.

3.4. X-Ray Absorption Fine Structure Spectroscopy

Fluorescence-yield Cr K-XAFS measurements were taken at room temperature on powdered soil samples. The samples were mounted in poly(tetrafluoroethylene) sample holders

and sealed with X-ray transparent Kaptan windows. Due to small sample quantities, the magnetic mineral fractions were contained between two layers of Kaptan tape only. Chromium K_{α} X-rays were collected through a 3-absorption-length V filter with a Stern-Heald ion chamber detector (Lytle et al., 1984). Transmission XAFS data were collected at room temperature for the chromite model and the mixtures of Cr(III) and Cr(VI) model compounds. The model compounds were mounted in Al sample holders, with enough sample mixed with X-ray transparent boron nitride to provide approximately one absorption length at the Cr K-edge energy. XAFS data were collected at the Stanford Synchrotron Radiation Laboratory (SSRL) on wiggler beamline 4-3 with a Si(220) $\phi = 0$ double-crystal monochromator. The electron storage ring was operated at 3 GeV and an electron current of 60–100 mA. The X-ray beam entering the monochromator was slit down to 1 mm \times 20 mm and a second set of slits in the sample hutch was set at 2 mm \times 20 mm. All spectra were calibrated in energy against the edge position of Cr(0) in a foil (16% Cr in austen steel) whose first inflection point is at 5989 eV. The harmonic content of the X-ray beam was eliminated by use of a 580 mm \times 30 mm \times 40 mm fused silica mirror coated with 1000 Å Pt so data could be collected with the X-ray beam fully tuned. Data from the Cr K-edge region (5980–6030 eV) were collected at 0.1 eV step size for high resolution of the pre-edge and edge features, and above the edge ($k = 1.62$ – 13 \AA^{-1}) the step size was 0.05 \AA^{-1} , with 0.7 s rest time between steps to minimize vibrational noise from monochromator crystal motion. Ion chambers placed before and after the sample were filled with N_2 , and the air path traveled by the X-ray beam before reaching the first ion chamber was bagged and filled with He, a gas much less absorbing than air at the Cr K-edge energy.

The choice of monochromator crystal is critical to XAFS edge studies such as this one. The Cr pre-edge peak resolution is significantly degraded when a Si(111) monochromator crystal is used. An attempt to use a different beamline, SSRL beamline 6-2, with a Si(111) monochromator crystal to study Cr in the soil samples and model compounds used in this study produced Cr(VI) pre-edge peaks that were broader and 30% lower in height than pre-edge peaks of the same samples collected on SSRL beamline 4-3 with a Si(220) monochromator crystal. Operating conditions at beamline 6-2 differed from those at beamline 4-3 in several ways. The monochromator crystal used at beamline 6-2 was Si(111), which has a d-spacing of 3.135 Å, whereas at beamline 4-3, a Si(220) monochromator was used which has a d-spacing of 1.920 Å. Achievable resolution is a convoluted function of the d-spacing of the monochromator crystal plane (e.g., Si(220) or Si(111)), the width of the crystal rocking curve, the size and collimation of the X-ray source, and the core-hole lifetime of the absorbing element (Brown et al., 1988; Lytle, 1989). The d-spacing of the monochromator crystal is inversely related to achievable resolution, making the Si(220) preferable over Si(111) for Cr K-edge studies. See (Farges et al., 1996) for a careful study on the effects of monochromator crystal type, monochromator slit size, and hutch slit size on the resulting resolution of Ti K-XANES features. Degradation in resolution may result from

X-ray beam focusing: a focused beam was used at beamline 6-2 which acted to degrade resolution by heating the monochromator crystal and inducing thermal noise in the data. To avoid this problem, an unfocused beam was used at beamline 4-3. Finally, beam brightness, or flux per unit of solid angle, is affected by the type of insertion device used (Brown et al., 1988), and beamline 6-2 has a 1 T, 54-pole wiggler insertion device whereas beamline 4-3 has an 1.8 T, 8-pole wiggler. No attempt was made in the current study to resolve the effects on resolution that were due to each factor, but the net result is that data collected on beamline 4-3 with the Si(220) monochromator crystal, Pt-coated mirror for harmonics rejection, and unfocused beam were optimal for high-resolution Cr K-XAFS data collection.

Monochromator crystal glitches, which are due to diffraction of the X-ray beam by the monochromator crystal and cause a sharp drop in the incident X-ray intensity recorded in the I_0 ion chamber, are also of concern for XAFS data collection. The Si(220) $\phi = 90$ cut has a broad glitch region over the k -range 10.2–11.7 \AA^{-1} making the Cr K-EXAFS data, especially data collected in transmission rather than fluorescence mode, unusable in this region. The Si(220) $\phi = 0$ cut, however, has only a small glitch appearing at $k = 8 \text{ \AA}^{-1}$ which can be easily removed during data analysis.

4. FUNDAMENTALS OF XAFS

The term X-ray absorption fine structure (XAFS) is used to refer collectively to both the X-ray absorption near-edge structure (XANES) and the extended X-ray absorption fine structure (EXAFS) regions. These two regions are differentiated on the basis of the dominant electronic processes in each region. At synchrotron X-ray energies in the Cr K-XANES region, the dominant process is multiple scattering. Multiple scattering occurs between outgoing and backscattered photoelectron waves between absorber Cr atoms and two or more surrounding atoms. In addition, multiple single-scattering events may occur, between the absorber Cr and a single nearby atom. At higher energies, in the Cr K-EXAFS region, single scattering dominates. Constructive and destructive interference between singly scattered outgoing and backscattered photoelectron waves causes most of the oscillatory EXAFS features. In addition, a prominent pre-edge peak at 5993.5 eV occurs when Cr is present as Cr(VI), caused by a bound-state 1s to 3d transition. This is a forbidden transition for octahedral Cr(III)O₆ which has a center of symmetry, but it is allowed for the noncentrosymmetric tetrahedral Cr(VI)O₄ molecule due to mixing of Cr(3d) and O(2p) orbitals. The empty d-orbital (3d⁰) of Cr(VI) increases the probability of the 1s to 3d transition, enhancing the pre-edge peak intensity (Fig. 1). The size of this pre-edge peak can be used to quantify the proportion of Cr(VI) in a sample if the Cr(VI) fraction makes up greater than ≈ 1 –5% of the total Cr present (Peterson et al., 1996b). Nevertheless, small pre-edge features are present for octahedral Cr(III) at 5990.5 and 5993.5 eV which are due to 1s to 3d(t_{2g}) and 1s to 3d(e_g) electronic transitions, respectively. The transition probability is increased by vibronic coupling, but Cr(III) pre-edge features are of low intensity because of the stability of the 3d³ electronic configuration

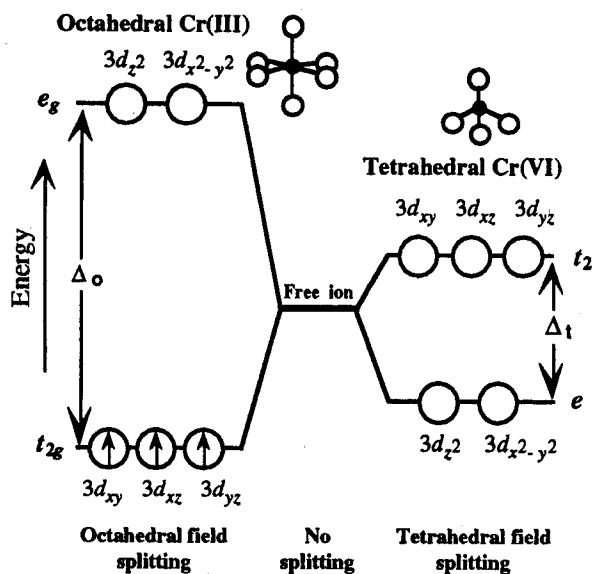


Fig. 1. Schematic illustration of octahedral crystal field splitting, Δ_o , of Cr(III)O_6 with d^3 electronic configuration, and tetrahedral crystal field splitting, Δ_t , of Cr(VI)O_4 which has an empty d orbital.

and the half-filled t_{2g} level of trivalent chromium (Fig. 1). The 3 eV separation of the Cr(III) pre-edge features agrees with the 2–3 eV octahedral crystal field splitting between the t_{2g} and e_g levels measured for several Cr(III) compounds in local octahedral coordination (Burns, 1993).

5. MODELING EXAFS DATA

XAFS data analysis was accomplished using the EXAFS-PAK suite of EXAFS analysis software (George, 1995), and theoretical modeling of experimental data was performed using the ab initio, single- and multiple-scattering code FEFF, v. 6.10 (Zabinsky et al., 1995). The phase and amplitude functions used in this study were derived from theoretical Cr(III) and Cr(VI) model compounds simulated using FEFF, and many of the theoretical models were also verified (Peterson et al., 1996a) by fitting experimental data collected on highly pure crystalline or solution samples of the same composition as the theoretical models. The experimental EXAFS spectra of Cr-containing model compounds were fit with FEFF phase and amplitude functions to evaluate the use of the same theoretical fitting procedure for Cr in unknown configurations on soil samples. This was done by fixing known N values (number of neighboring atoms), verifying that the resulting R values (distance, Å, from the absorber Cr atom) were accurate to within 0.03 Å, and verifying that the phase and amplitude functions for the appropriate backscatterer atom, i.e., Cr, O, Si, etc., gave good fits to the experimental model compound data. Fits to natural soil sample EXAFS data, therefore, are assumed to be accurate to ± 0.03 Å, based on results of fits to experimental model compound EXAFS data. Debye-Waller factors, used to simulate static and vibrational atomic disorder, were constrained using theoretical fits to model compounds. Experimental Cr(III) model compounds used in this study include FeCr_2O_4

(chromite) and Cr_2O_3 ; experimental Cr(VI) models used include $\text{Na}_2\text{CrO}_4 \cdot 4\text{H}_2\text{O}$ and CaCrO_4 . Theoretical models were made of all the experimental compounds using ATOMS, v. 2.42d (Ravel, 1995). Theoretical model structures were also made of the Cr(III) compounds α -, β -, and γ - CrOOH and the Cr(VI) compounds $\text{Ca}(\text{Cr,S})\text{O}_4 \cdot 2\text{H}_2\text{O}$ (Cr-substituted gypsum) and CrPbO_4 (crocoite) for use in fitting experimental XAFS spectra. The Cr-substituted gypsum was simulated using ATOMS by substituting a Cr atom in the symmetry position normally occupied by S.

6. RESULTS AND DISCUSSION

6.1. Mineral Characterization

6.1.1. Keyport soils

Keyport soil samples were found to contain 380–1195 $\mu\text{g g}^{-1}$ Cr. These levels are much higher than uncontaminated soils which contain, on average, 50 $\mu\text{g g}^{-1}$ Cr (O'Neill, 1985). Keyport soil mineralogy is dominated by quartz, K-feldspar, and plagioclase feldspar, identified by X-ray diffraction (XRD), with accessory pyroxene and magnetite, identified by electron microprobe. The magnetite fraction of the Keyport soil samples (1.6 ± 0.8 wt%) was isolated from the bulk by magnetic separation.

6.1.2. Sandia soils

Samples collected at Sandia Cr disposal pits contain far more Cr, up to 20,700 $\mu\text{g g}^{-1}$. The highest Cr content (20,700 $\mu\text{g g}^{-1}$) was measured at a disposal pit used in the 1970s, followed by 16,500 $\mu\text{g g}^{-1}$ Cr measured at a 1980s pit, and up to 8,000 $\mu\text{g g}^{-1}$ Cr measured in a 1960s pit. At the 1960s disposal pit, total Cr was found to be highly correlated with Pb and SO_4 , and at depths greater than 8 m, Cr(VI) content is also correlated with SO_4 content in twenty depth-increment analyses over a 30-m depth profile cored through the unlined pit (Fig. 2). Spikes in total Cr content at 8 and 16 m are echoed by spikes in Pb and SO_4 at the same depths in the soil profile. Sandia soil mineralogy is dominated by quartz (71% by XRD) and feldspar (16% plagioclase and 3% potassium feldspar) with $\approx 5\%$ each of calcite and clay minerals with 10 Å interlayer spacing (Stein et al., 1994). Magnetite from Sandia soil samples, identified by magnetic separation and electron microprobe analysis, varied in quantity from below detection (1960s pit) to 1.5 ± 0.5 wt% (1970s and 1980s pits). Total organic carbon was measured to be 0.35 wt%.

6.2. Chromium at Mineral Surfaces

X-ray photoelectron spectroscopy (XPS) measurements were carried out on a subset of the Keyport nonmagnetic (predominantly quartz and feldspar) and magnetic mineral separates to verify that the Cr present in the samples was at or near the mineral surfaces. It is likely that part of the Cr XAFS signal is from structural Cr in the magnetites, as Cr^{3+} is commonly found to substitute for Fe^{3+} in the magnetite (Fe_3O_4) structure. Surface layers of the mineral separates were progressively removed with Ar ion sputtering. The XPS peak area of Cr2p (the sum of the $\text{Cr}2p_{3/2}$ and $2p_{1/2}$ peak

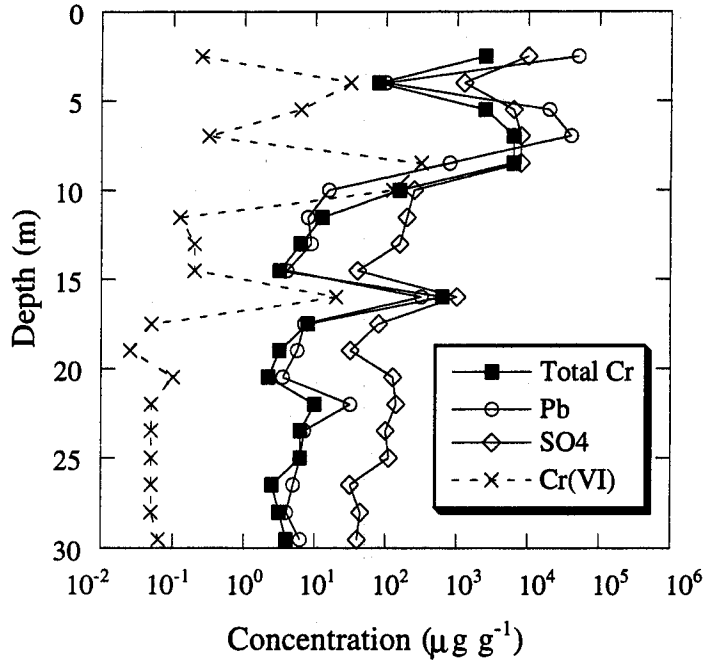


Fig. 2. Concentrations of total Cr, Pb, SO₄, and Cr(VI) with depth for the Sandia 1960s waste disposal pit. The sample for XAFS analysis was taken from the 3.5 m interval. Analyses were performed by Enseco, a division of Corning Laboratory Services, Inc.

areas), normalized to Fe2p (the sum of the Fe2p_{3/2} and 2p_{1/2} peak areas), dropped off with sputter depth for the magnetite sample (Fig. 3). This analysis does not rule out the presence of Cr in the bulk, but it indicates the concentration of Cr at

or near the magnetite surface. The surface of the Keyport soil quartz + feldspar fraction was also sputtered, and a decrease in the Cr2p peak area, normalized to the Si2p peak area was observed, but only after an initial rise in the Cr/Si

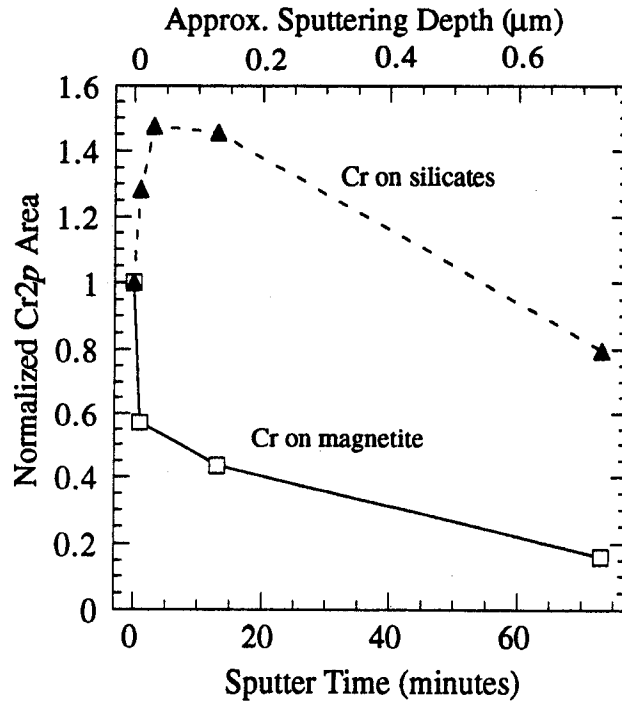


Fig. 3. XPS depth profiles of Cr2p peak areas of the K-1 Keyport soil mineral separates normalized to Fe2p peak area (magnetite fraction; squares) and Si2p peak area (quartz + feldspar mineral fraction; triangles).

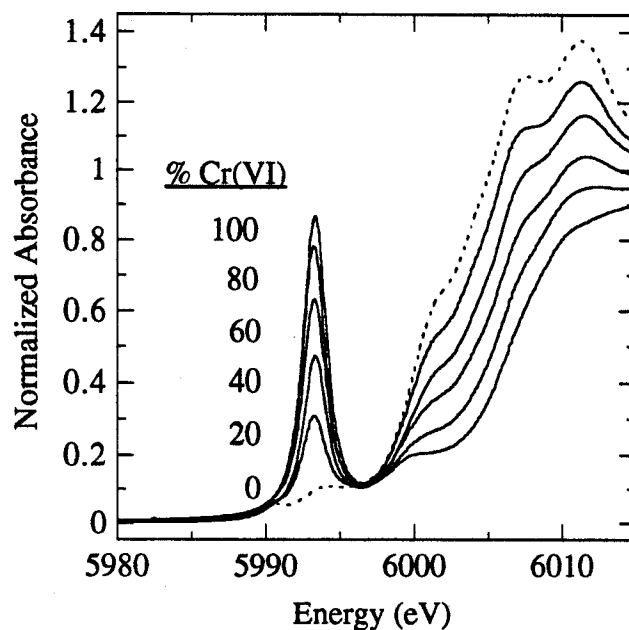


Fig. 4. Normalized pre-edge region of mixtures of Cr(III) + Cr(VI) in mol% ratios. The 100% Cr(III) endmember (Cr_2O_3) spectrum is dotted to illustrate the relationship between edge position, edge shape, pre-edge height and Cr(VI):Cr(III) ratio. Increasing pre-edge height reflects increasing Cr(VI) content ($\text{Na}_2\text{CrO}_4 \cdot 4\text{H}_2\text{O}$).

peak ratio (Fig. 3). The immediate drop in the XPS Cr signal on magnetite vs. an initial increase then decrease in the XPS Cr signal on silicates can be attributed to the sample preparation procedure. Because of limited sample quantity, the magnetic fraction of the soil was the same as that used for XAFS analysis, and had been powdered, so the exposed surfaces for XPS analysis were mostly fresh surfaces. The quantity of the silicate fraction was not a limiting factor, so XPS sputtering was carried out on natural, unpowdered grains. Natural grains have irregular surface topography and associated surface layers of clays and small particles which had to be sputtered through, explaining the initial rise in the Cr/Si ratio before the Cr signal peaked. Chromium(III) and Cr(VI) content were not determined by XPS peak fitting routines because of low signal-to-noise in the Cr2p XPS signal for both the silicate and magnetic fractions.

6.3. Pre-Edge Peak Calibration

To use the Cr K-XAFS pre-edge peak in quantifying the Cr(VI)/total Cr content of Cr-contaminated soil samples, the pre-edge peak height was calibrated by examining the pre-edge region of a series of model compounds containing known amounts of Cr(III) and Cr(VI) (Peterson et al., 1996b). The background-subtracted peak area was found to provide almost exactly the same fit to the data as peak height, so for ease of measurement we chose to measure peak height. The background-subtracted pre-edge height vs. Cr(VI) content data (Fig. 4) are well fit with a second-order polynomial function (Fig. 5; $R = 0.998$), with an accuracy of $\pm 3\%$ when compared to the known Cr(VI)/total Cr values (Table 1). Other researchers have postulated a linear pre-edge height trend (Bajt et al., 1993) based on measured peak area

and normalization to the absorbance at 400–500 eV above the edge jump. However, when this method was applied to our data, the correlation between peak size and Cr(VI) content was worse than the procedure we have adopted. A probable explanation is that even several hundred eV above the edge there are EXAFS features that cause oscillation of the absorbance values, making any single datum unreliable as a normalization point. In addition, there is often an overall increase or decrease in absorbance with increasing energy in the EXAFS region even after background subtraction, so there may not be a region of unchanging absorbance in the EXAFS region of the dataset to provide a data normalization point. An attempt was made to normalize the pre-edge height to various sample absorbance values near the edge jump, in the XANES rather than in the EXAFS region, and a linear trend in peak height vs. Cr(VI) content was produced. However, most fits obtained using this approach were poor. Data normalization methods which use actual data points, rather than a point on a spline fit to the data, are highly dependent on the data and are not universally applicable.

The proper method of normalizing XAFS data, so that the pre-edge height is not a function of total Cr present or oscillations in absorbance values, is to subtract the pre-edge background from the data, then fit a spline function to the XAFS and extrapolate this function to the main edge energy (Brown et al., 1988; Farges et al., 1996). The XAFS data are then normalized to an edge jump defined by the difference in pre-edge background and the height of the spline at a normalization point selected near the edge. The normalization point for Cr XAFS data was chosen to be 6030 eV.

For comparison with other XAFS data in the literature, several methods of spline-fitting the data were examined. In each case, a spline region from 6005 eV to the end of the

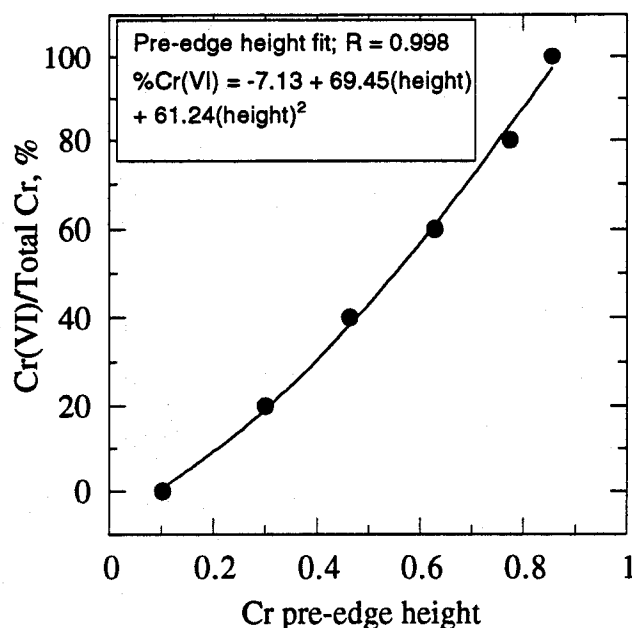


Fig. 5. Chromium(VI) content vs. pre-edge peak height of the Cr(III) and Cr(VI) mixtures of Fig. 4 and a second-order polynomial fit to the data. A plot of pre-edge peak area rather than height shows the same trend in the data.

dataset was selected, with k^4 weighting for the spline, and three spline ranges. Any normalization point on the spline in the XANES region above the edge jump (i.e., 6015–6030 eV) resulted in fits indistinguishable from that presented in Fig. 5. Normalization points selected in the EXAFS region resulted in an irregular trend of pre-edge height with Cr(VI) content, so this approach was rejected. Moving the lower boundary of the spline region from 6005 eV, just below the top of the edge jump, to a point a few eV above the edge jump did not yield a statistically significant improvement in the resulting R value over that obtained with spline range beginning at 6005 eV, so this approach of spline fitting was also rejected.

In addition to pre-edge peak height measurement, three other XAFS methods were tested for Cr(VI)/total Cr content determination on the Cr(III) and Cr(VI) model compound mixtures. The first method relies on the difference in local coordination geometry of Cr in its two common oxidation states. Trivalent Cr is octahedrally coordinated, with six oxygen atoms at ≈ 2 Å, whereas hexavalent Cr is tetrahedrally coordinated, with four oxygen atoms at ≈ 1.6 Å. Ab

initio fits to the EXAFS based on FEFF models of the components (Cr_2O_3 and Na_2CrO_4) give the proportion of oxygen atoms at ≈ 1.6 Å, the Cr(VI) O_4 fraction, and the proportion of oxygen atoms at ≈ 2.0 Å, the Cr(III) O_6 fraction. A second method tested for determining Cr(VI)/total Cr content uses the endmember Cr(III) and Cr(VI) EXAFS spectra to fit the EXAFS spectra of the Cr(III/VI) mixtures. The third method uses the endmember Cr(III) and Cr(VI) XANES to fit the Cr(III/VI) XANES mixtures. A tabulation of the resulting Cr(VI) contents calculated from each of these methods (Table 1) shows that the normalized pre-edge height method reproduces the known Cr(VI)/total Cr content to $\pm 3\%$, while the ab initio EXAFS fitting method is accurate to $\pm 8\%$; the endmember Cr(III) EXAFS and Cr(VI) EXAFS fitting is accurate to $\pm 7\%$, and endmember Cr(III) XANES and Cr(VI) XANES fitting is accurate to $\pm 6\%$. Accuracy in this test is defined as the difference between the calculated fraction of Cr(VI), as determined by each of four methods, and the known fraction of Cr(VI) in mixtures of the models Cr_2O_3 and Na_2CrO_4 that were mixed in molar ratios using an analytical balance. Thus, Cr(VI)/

Table 1. Cr(VI) content, relative to total chromium, calculated by several XANES and EXAFS fitting methods.

Known Cr(VI) fraction, mole %	Cr(VI) % by Pre-edge height	Cr(VI) % by ab initio EXAFS fitting	Cr(VI) % by end-member EXAFS fitting	Cr(VI) % by end-member XANES fitting
100	97	100	100	100
80	83	79	89	84
60	61	64	67	66
40	38	47	47	46
20	19	28	25	24
0	0.7	0	0	0

Table 2. Cr(VI) content relative to total chromium, determined by calibrated pre-edge height.

Sample	Cr(VI)%
Keyport, WA site	
K-1, nonmagnetic fraction	6.4
K-1, magnetite fraction	n.d.*
K-3, nonmagnetic fraction	5.6
K-3, magnetite fraction	n.d.
K-4, nonmagnetic fraction	0.8
K-4, magnetite fraction	n.d.
Sandia, NM site	
1960s pit, nonmagnetic fraction	66.9
1980s pit, nonmagnetic fraction	32.8
1980s pit, magnetite fraction	32.7
1970s pit, nonmagnetic, 1987 [†]	7.2
1970s pit, nonmagnetic, 1992 [†]	7.3
1970s pit, magnetite, 1992 [†]	2.2

* not detected

[†] sampling date

total Cr content may be most accurately determined among the methods tested by measuring the normalized pre-edge peak height. This method also requires the least data manipulation.

6.4. Chromium Oxidation State by Pre-Edge Height

6.4.1. Keyport soils

When the pre-edge height calibration curve is applied to the normalized pre-edge peaks of Cr-containing soils from Keyport, the results show Cr(VI)/total Cr contents of 0–6.4% (Table 2). Keyport magnetites contain no measurable Cr(VI), and their pre-edge features (Fig. 6, XANES, curves b, d, and f) are similar, but not identical, to the pre-edge of a Cr(III) model (Fig. 4, dotted line), with a sharply-defined edge jump maximum at 6010 eV. The quartz + feldspar fractions of Keyport soils contain up to 6.4% Cr(VI) relative to total Cr (Fig. 6, curves a, c, and e), as reflected by the presence of a small pre-edge peak, as well as an overall edge shape that more closely resembles the XANES of a mixture of Cr(III) and Cr(VI); see Fig. 4. The pairs of mineral separate XAFS are plotted according to decreasing Cr(VI) content in the nonmagnetic fraction for three Keyport soil samples K-1 (Fig. 6a and b), K-3 (Fig. 6c and d), and K-4 (Fig. 6e and f). Chromium(VI)/total Cr content does not correlate with total Cr, however, as K-3 has the highest total Cr (1195 $\mu\text{g g}^{-1}$), followed by K-1 (615 $\mu\text{g g}^{-1}$) and K-4 (380 $\mu\text{g g}^{-1}$), whereas the trend in Cr(VI)/total Cr begins with K-1 having the highest Cr(VI)/total Cr content (6.4%), followed by K-3 (5.6%), then K-4 (0.8%); Table 2.

6.4.2. Sandia soils

Sandia samples contain even more Cr(VI) than do Keyport samples: between 2.2 and 67% of the total Cr is present as the more toxic, and potentially more mobile, hexavalent form of Cr (Table 2), as determined by calibrated pre-edge height. The pre-edge data, presented in order of decreasing

Cr(VI) content (Fig. 7, XANES) show that, in contrast to samples from Keyport, the Sandia samples are highly variable in Cr(VI)/Cr(III) ratios. Where possible, magnetite was separated from the bulk sample and analyzed separately (Fig. 7c and f). In contrast to the distinct differences seen in the XANES of Keyport nonmagnetic vs. magnetite mineral fractions, a comparison of nonmagnetic and magnetite fractions from the Sandia 1960s pit (Fig. 7b and c) shows little difference between pre-edge height, edge position, and edge shape. The similarity between the XANES of the magnetite and silicate mineral fractions may be attributed to several possible causes: (1) the 1960s pit sample has seen more Cr(VI) than was reducible by the trace quantities of magnetite present, (2) with the abundance of Pb also present in this disposal pit, the relative kinetics of CrPbO₄ precipitation vs. Cr(VI) reduction by magnetite may favor the CrPbO₄ precipitation, and (3) the surfaces of magnetites at this site may have been oxidized and passivated, therefore, no longer capable of Cr(VI) reduction. This last process was observed to occur for Cr(VI) reacting at neutral pH with synthetic magnetite in laboratory experiments by Peterson et al. (1997). Possibly, all of these scenarios occurred in the 1960s pit, but a lack of relevant kinetic data precludes resolution of their relative importance. Samples from the 1970s pit, however, do show distinct differences in Cr(VI)/total Cr content between the nonmagnetic and magnetite fractions (Fig. 7e and f) and have quite different pre-edge height, edge position, and edge shape. Like the Keyport silicate vs. magnetite fractions, the Sandia 1970s pit XANES shows a larger pre-edge peak in the quartz + feldspar mineral fraction as contrasted to the magnetic mineral fraction, indicating that some of the Cr(VI) has been reduced to Cr(III) by electron transfer from Fe²⁺ in the magnetite substrate. The edge shape of the 1970s pit magnetite fraction shows a sharply defined edge peak at 6010 eV, more closely resembling Cr(III) model XANES, in contrast to the more rounded edge peak of the quartz + feldspar fraction, reflecting the mixed oxidation states present.

6.5. Chromium Oxidation State by Edge Position

6.5.1. Keyport soils

Close examination of the edge position of the Keyport silicate XANES spectra also reveals the presence of Cr in mixed 3+ and 6+ oxidation states. While the edge position of Keyport magnetites, 6000.8 eV, measured at half the normalized edge-jump height (Fig. 4, dotted line), is close to that of the Cr(III) model, the edge position of Keyport silicate samples was shifted higher by 0.2–1.4 eV, with the larger shift in edge position occurring with the higher Cr(VI)/total Cr content of the sample (given in Table 1). Edge positions at half the normalized edge-jump height are, in order of increasing Cr(VI)/total Cr content for Keyport silicate fractions: 6001.0 eV for K-1 with 0.8% Cr(VI)/total Cr, 6001.8 eV for K-3 with 5.6% Cr(VI)/total Cr, and 6002.2 eV for K-4 with 6.4% Cr(VI)/total Cr (Fig. 6, XANES). This trend is consistent with the shift in edge position observed for mixtures of Cr(III) and Cr(VI) model compounds (Fig. 4).

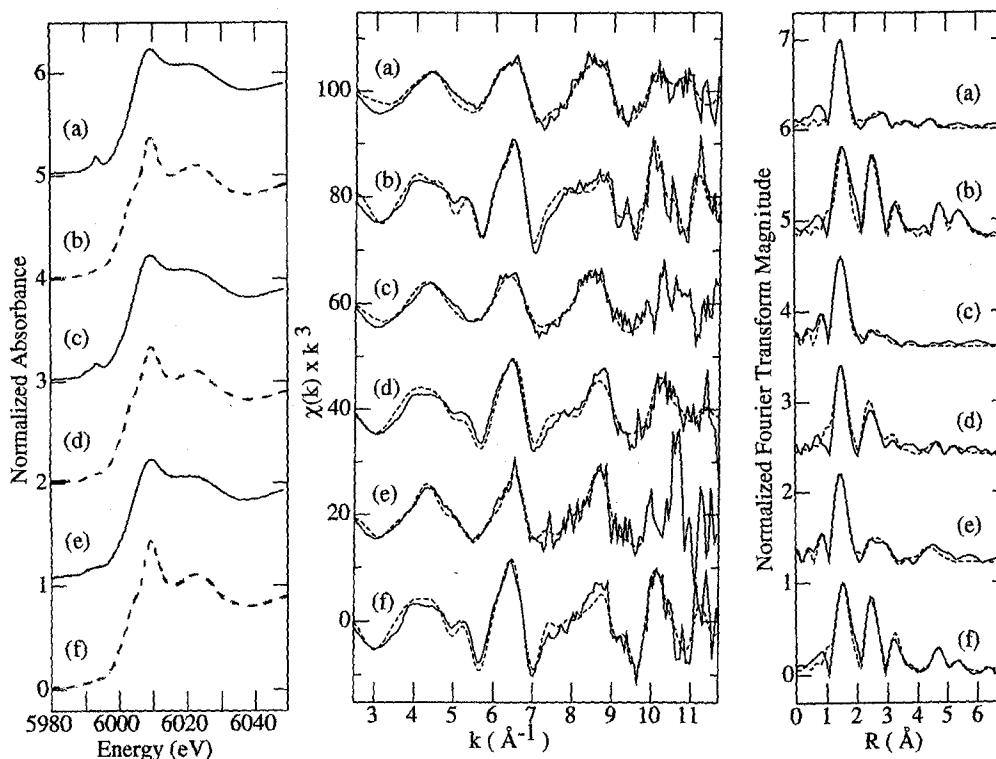


Fig. 6. Chromium K XANES (left), EXAFS (center), and Fourier transformed EXAFS (right) of pairs of Keyport nonmagnetic (curves a, c, and e) and magnetite (curves b, d, and f) mineral separates. The XANES of Cr sorbed on the nonmagnetic (quartz + feldspar) fractions (left; curves a, c, and e) show minor pre-edge peaks at 5993 eV due to 0.8–6.4% Cr(VI)/total Cr; XANES of Cr sorbed on the magnetite fraction (left; curves b and d) have pre-edge features characteristic of Cr(III). EXAFS data (center; solid lines) were fit (center; dashed lines) over $k = 2.5$ – 11.7 \AA^{-1} except for c and e whose EXAFS were fit over $k = 2.5$ – 9.8 \AA^{-1} due to noise at high k . Fourier transforms (right; solid lines) and fits (right; dashed lines) were performed over the same k ranges.

6.5.2. Sandia soils

The edge positions of the Sandia samples also shift with Cr(VI)/total Cr content. With increasing pre-edge height there is a corresponding shift in the edge position, measured at half the normalized edge-jump height, due to the increasing Cr(VI) content: the 1970s pits have 2.2% (magnetic fraction) and 7.2% (nonmagnetic fraction) Cr(VI)/total Cr with corresponding edge positions of 6001.6 eV (magnetic fraction) and 6002.0 eV (nonmagnetic fraction) (Fig. 7, XANES); both the magnetic and nonmagnetic fractions from the 1980s pit have 33% Cr(VI)/total Cr and a higher edge position (6003.0 eV); and the 1960s pit has the highest Cr(VI)/total Cr content (67%) and the highest edge position (6005.3 eV).

6.5.3. Chromium model compounds

Edge positions of the model compound mixtures (Fig. 4), measured at one half of the normalized edge jump absorbance, are 6000.3, 6001.0, 6003.0, 6004.0, 6005.3, and 6006.4 eV for 0, 20, 40, 60, 80, and 100% Cr(VI)/total Cr contents, respectively. This increase in edge position energy with increasing Cr(VI)/total Cr is consistent with the edge-shift observed for the Cr-contaminated soil samples. Edge position, without knowledge of the local geometry of each

phase present, should not be used for determining Cr(VI) content, however, because the XANES shape results from a combination of bound-state as well as continuum-state electronic transitions, and both single- and multiple-scattering features. The multiple scattering paths that affect edge structure are highly dependent on the identity of Cr phases present and their local geometry, and for these natural soils there may be multiple phases of each Cr oxidation state present. XANES of several Cr(III) and Cr(VI) mineral and solution model compounds show that the edge position is variable, even for model compounds containing Cr in the same oxidation state (Peterson et al., 1996a). The general shift in edge position, however, may be used as a qualitative indication of the presence of trivalent, hexavalent, or mixed-valence Cr species.

6.6. Chromium in Magnetites vs. Chromium on Silicates

6.6.1. Keyport soils

Chromium is present in multiple phases—in minerals, precipitate phases, and/or sorption complexes—in all of the natural soil samples examined. Fits to the Keyport EXAFS spectra of the mineral separates (nonmagnetic and magnetite fractions) revealed distinct differences in local Cr geometry

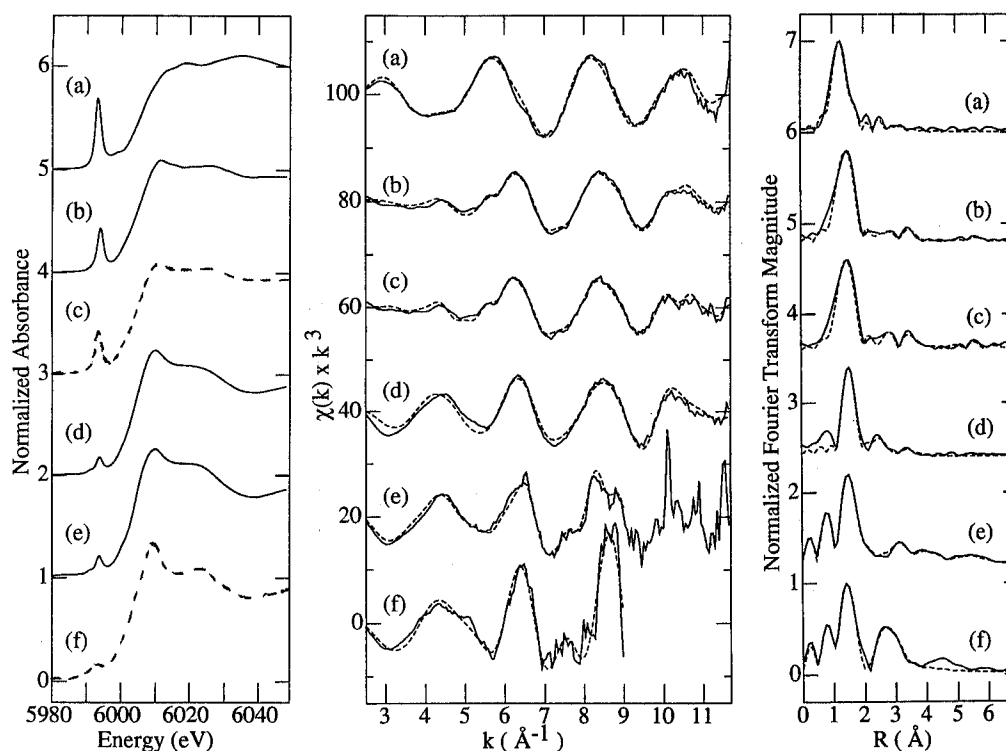


Fig. 7. Chromium K XANES (left), EXAFS (center), and Fourier transformed EXAFS (right) of Sandia soil samples in order of decreasing Cr(VI)/total Cr content: (a) 1960s disposal pit, nonmagnetic fraction; (b) 1980s pit, nonmagnetic fraction; (c) 1980s pit, magnetite fraction; (d) 1970s pit (sampled 1987), nonmagnetic fraction; (e) 1970s pit (sampled 1992), nonmagnetic fraction; (f) 1970s pit (sampled 1992), magnetite fraction. XANES (left) of nonmagnetic fractions (dominantly silicate minerals) are curves a, b, d, and e; XANES of magnetite fractions are curves c and f. EXAFS data (center; solid lines) were fit (center; dotted lines) over $k = 2.5\text{--}11.7 \text{ \AA}^{-1}$ except for e and f whose EXAFS were fit over $k = 2.5\text{--}9.0 \text{ \AA}^{-1}$ due to noise at high k . Fourier transforms (right; solid lines) and fits (right; dotted lines) were performed over the same k ranges.

as a function of the substrate (Fig. 6, EXAFS). A contribution to the EXAFS from Cr(III)-O at $1.97 \pm 0.05 \text{ \AA}$ is present in both the nonmagnetic (quartz + feldspar) and magnetite mineral fractions. This is consistent with the presence of Cr(III)O₆ octahedra which exist in every Cr(III) oxide and oxyhydroxide phase. Chromium(VI)-O is also present in the silicate fractions, but not the magnetite fractions, at $1.65 \pm 0.01 \text{ \AA}$, consistent with the presence of Cr(VI)O₄ tetrahedra, the local structure about Cr(VI) in oxides and salts. There is also a contribution to the Keyport magnetite-fraction EXAFS from Cr(III)-O multiple scattering along a triangular path between Cr and two nearest oxygen atoms at $3.19 \pm 0.03 \text{ \AA}$. These multiple scattering paths may also be present in the silicate fractions, but the addition of a multiple scattering component has a negligible effect on the resulting fits to the silicate EXAFS.

6.6.2. Keyport magnetite fraction

Beyond the first oxygen shell(s), the identity and distances of neighboring atoms surrounding Cr differ markedly as a function of the mineral fraction with which the Cr is associated. Chromium associated with the magnetite fraction of the Keyport samples is dominantly in a local coordination geometry consistent with that of chromite (Fe-

Cr₂O₄) or Cr-substituted magnetite (Fe_{3-x}Cr_xO₄) or a combination of the two phases. The Cr-Cr/Fe distances (R , \AA) found by fitting EXAFS spectra for the magnetite fractions of samples K-1, K-3, and K-4 ($R = 3.0 \pm 0.02$, 3.49 ± 0.05 , 5.18 ± 0.05 , and $5.53 \pm 0.07 \text{ \AA}$) are consistent with chromite Cr-Cr distances (2.96 , 5.13 \AA) and Cr-Fe distances (3.47 , 5.44 \AA), suggesting that the Cr may be present as a chromite phase. The Cr-Cr/Fe distances are also consistent with Fe(oct)-Fe(tet, oct) distances of magnetite (2.97 , 3.48 , 5.14 , and 5.45 \AA), suggesting, alternatively, that the Cr may be sorbed to the magnetite surface at sites where octahedral Fe³⁺ atoms would be if the magnetite structure were not terminated by the surface, or that the Cr is present in the bulk of the magnetite as Cr³⁺ substituted for octahedral Fe³⁺. Similar local structure was observed by XAFS analysis for Cr(VI) reduced to Cr(III) and sorbed on magnetite in a laboratory investigation (Peterson et al., 1996a). The similarity in backscattering phase and amplitude functions of Cr and Fe unfortunately precludes using EXAFS to resolve which phase or phases may be present: a chromite precipitate, Cr sorbed at octahedral Fe sites on magnetite, Cr-substituted magnetite, or a mixture of these phases. The presence of significant quantities of other Cr(III) phases such as Cr₂O₃ or CrOOH may be ruled out, however, both by the fitted R -values and by visual

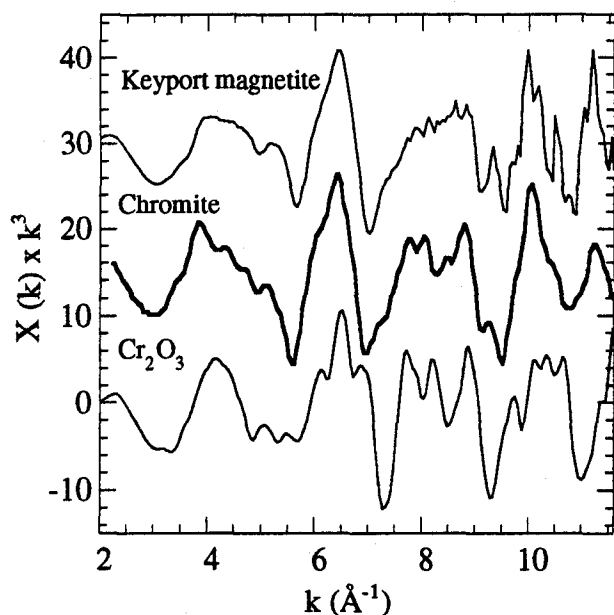


Fig. 8. EXAFS spectrum of the Keyport K-1 magnetite fraction containing 6.4% Cr(VI)/total Cr and two model compound EXAFS spectra. The model data for chromite (FeCr_2O_4 ; bold) are very similar to the Cr associated with the Keyport magnetite, whereas the chromium oxide (Cr_2O_3) data appear quite different. The EXAFS of other models such as CrOOH have even fewer similarities to the experimental Keyport magnetite EXAFS data.

comparison of the experimental data with EXAFS and Fourier transformed EXAFS of various models (Figs. 8, 9).

Quantitative electron microprobe analysis of several Keyport magnetite grains yielded a range of Cr contents of the magnetites: from ≤ 0.03 wt%, the microprobe detection limit for Cr, to 0.18 ± 0.01 wt% Cr. Isolated chromite grains in the magnetic mineral fraction were also identified, containing 25 ± 0.2 wt% Cr. Microprobe analysis excites electrons from a region appropriate in size for bulk mineral or precipitate phase identification, but it cannot detect sorbed species present in monolayer or submonolayer thicknesses, or indeed, surface coatings thinner than $\approx 0.1 \mu\text{m}$. Therefore, the microprobe is highly useful as an adjunct to XAFS analysis in corroborating the presence of Cr precipitate phases on the soil minerals, but it cannot confirm or preclude the presence of sorbed phases. Since the pre-edge region of Keyport magnetites resembles that of Cr(III), and model compound analysis indicates that Cr(VI) should be detectable if present at concentrations greater than $\approx 1-5\%$ of the total Cr (Peterson et al., 1996b), we conclude that the Cr effluent at the Keyport site has been reduced from mixed Cr(VI) + Cr(III) to dominantly Cr(III) at the magnetite surface. Chromium remains present in a mixed Cr(III) + Cr(VI) state when associated with the silicate fraction, so a model for Keyport soils that is consistent with the data is one in which the mixed oxidation state Cr waste reacted with the magnetite grains and was reduced to Cr(III) by electron transfer from Fe^{2+} in magnetite, whereas the Cr waste reacted with silicates remained dominantly unchanged in oxidation state. This hypothesis is consistent with the pre-edge and XANES data for

the magnetite fractions, which show characteristic Cr(III) features, and the pre-edge and XANES data for the silicate fractions, which show mixed Cr(III) and Cr(VI) features.

Reduction of Cr(VI) to Cr(III) by magnetite could be an intrinsic remediation process, i.e., a natural process where no intervention, such as ground water extraction and treatment, is required to reduce Cr(VI) levels. As shown by the lingering presence of Cr(VI) on the silicate fraction of Keyport soils, however, the quantities of magnetite present in these soils are too low for this natural process to be effective for site-wide natural remediation.

6.6.3. Keyport silicate fraction

Chromium sorbed to the silicate fraction of the Keyport samples K-1, K-3, and K-4 is present as both Cr(VI) and Cr(III) and shows marked differences in sorption geometry when compared to the magnetite fraction. EXAFS fits showing the presence of Cr-Cr at 3.02 ± 0.03 and 3.88 \AA (Fig. 6a, c, e) are consistent with the presence of a γ - CrOOH precipitate on the silicate minerals (edge-sharing CrO_6 octahedra with Cr-Cr at 3.0 \AA and corner-sharing octahedra with Cr-O at 3.9 \AA) as seen, also by EXAFS spectroscopy, on smectite (Corker et al., 1991), on silica (Fendorf et al., 1994), and, mixed with α - CrOOH , on hydrous ferric oxide and goethite (Charlet and Manceau, 1992). Contributions to the EXAFS from Si or Al are also noted, with Cr-Si/Al distances of 3.55 ± 0.08 and 4.9 \AA . As for Cr and Fe, Si and Al are difficult to distinguish by EXAFS because of the similarity of their phase and amplitude functions. The presence of Si or Al, nevertheless, indicates that the (alumi-

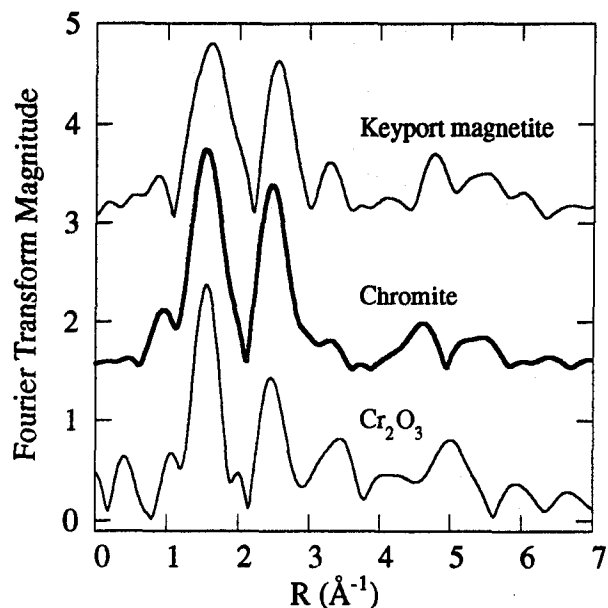


Fig. 9. Fourier transformed EXAFS of the Keyport K-1 magnetite fraction containing 6.4% Cr(VI)/total Cr and two model compounds showing the similarities in Fourier transform peaks between the Keyport magnetite fraction and the chromite model (bold); in contrast the Fourier transformed EXAFS of the Cr_2O_3 model has peaks in positions which do not correspond to those of the Keyport sample.

no)silicate substrate is in close proximity to the Cr atoms. The proposed model of Cr(III) sorption based on these fits is that Cr is sorbed on the silicate minerals, with a local structure like that of γ -CrOOH, but with evidence of the substrate atoms present beyond the first shell of metal atoms around the Cr. In addition to Cr(III), a measurable amount of Cr(VI) is also present. The identity of the Cr(VI) phase may not be determined by this method because of the weak backscattering of Cr(VI) neighbor atoms at distances larger than that of the first shell of oxygens, combined with the low proportion of Cr(VI) relative to Cr(III). Microprobe results suggest that Cr is present in association with Pb as a precipitate phase on quartz and plagioclase feldspar grains. Consideration of Cr-Pb backscattering does not improve fits to the Keypoint XAFS data. This result suggests that Cr and Pb phases may be associated in the Keypoint samples at the scale of microprobe analysis ($>1 \mu\text{m}$), but these phases do not appear to be intimately associated at the Angstrom scale resolvable by XAFS.

6.7. EXAFS Identification of Precipitate Phases

6.7.1. Sandia 1960s pit

Sandia samples come from chemical waste disposal pits used predominantly for metal plating waste containing a significant concentration of Cr and sometimes Pb. The resulting Cr complexes precipitated on the soil minerals are highly variable in Cr content, oxidation state, and structure. The 1960s pit sample is dominated by Cr(VI), with 67% of the Cr present as Cr(VI) (Table 2). Total Cr content of this unlined pit varies inversely with depth, from 5–10 $\mu\text{g g}^{-1}$ at 18–30 m depth to 8000 $\mu\text{g g}^{-1}$ in shallower parts of the core. FEFF fits to the EXAFS of a sample from this pit (Fig. 7a) reveal the presence of Cr(VI)-O backscattering at 1.64 Å distance, Cr(III)-O at 2.01 Å, Cr-Cr at 2.87 Å, Cr-Ca at 3.17 Å, and Cr-Pb at 3.38 Å. In addition, multiple-scattering from Cr and O in Cr(III)O₆ octahedra contributes at 3.80 Å. A model of Cr-bearing phases consistent with these fits includes Cr(VI) in both CaCrO₄ and CrPbO₄, plus Cr(III) in Cr₂O₃ with the Cr-O multiple scattering component also arising from this phase. The high Cr content of this sample caused a very strong EXAFS signal with low noise content so that the normally weakly backscattering phases such as Cr(VI) salts and oxides could be identified. Microprobe results confirm the presence of a Cr-Pb oxide phase, present both as isolated rhombic crystals and as surface coatings on quartz grains. Microprobe analysis also found a precipitate phase on quartz grains in which Cr, Pb, and Ca were all present, consistent with XAFS results suggesting the presence of Cr(VI) phases CaCrO₄ and CrPbO₄.

The sample used for XAFS analysis from the Sandia 1960s pit was from a subsurface depth of 3.5 m. Lead and total Cr were found to be highly correlated with depth over the entire 30 m length of the core, and this result is entirely consistent with the XAFS determination of a CrPbO₄ phase. At depths greater than 9 m, SO₄ and Cr(VI) were found to be highly correlated, suggesting that the Cr(VI) may be present at these depths in the core as a Cr-containing sulfate phase. Microprobe analysis of the 3.5 m sample confirmed

the presence of a PbSO₄ phase, but Cr is not highly concentrated in this phase. When Cr is present in the 3.5 m depth increment sample, it is dominantly present as a Cr-Pb oxide, consistent with analyses done on the 0–9 m depth increments of the core, where SO₄ and Cr(VI) are not correlated.

6.7.2. Sandia 1980s pit

The Sandia 1980s pit sample contained 16,500 $\mu\text{g g}^{-1}$ total Cr, 33% of which is present as Cr(VI) (Table 2). This soil sample was divided into magnetic and nonmagnetic fractions, and the EXAFS spectra were nearly identical for both fractions (Fig. 7b and c). Possible reasons for the similarity have been discussed previously (section 6.4.2). FEFF fits (Fig. 7b, c) indicate that Cr(VI)-O is present at 1.63 Å, along with Cr(III)-O at 1.99 Å, and Cr-Cr at 2.68, 3.43, 3.63, 5.55, and 6.11 Å. Chromium-oxygen multiple scattering was also fit to the EXAFS at 3.86 Å from three-leg paths in the Cr(III)O₆ octahedra. The Cr(VI) phase could not be identified by XAFS analysis due to the weak backscattering of its surrounding atoms beyond the oxygen shell, but microprobe analysis verified that a Cr-Ca phase, CaCrO₄, was present rimming many of the mineral grains. The Cr(III)-O and Cr-Cr distances from EXAFS fitting are consistent with Cr(III) in Cr₂O₃, which by XRD gives Cr-O distances at 1.96 and 2.02 Å and Cr-Cr distances at 2.65, 3.43, and 3.65 Å (Newnham and de Haan, 1962), which agree to ± 0.03 Å with EXAFS fits to these samples. XRD-derived Cr-Cr distances of 5.36, 5.63 Å, and 6.16 Å for Cr₂O₃ agree to ± 0.05 Å with EXAFS fits to these samples. Several Cr-Cr distances between 3.6 and 6.1 Å, known from theoretical modeling of the Cr₂O₃ structure and XRD-derived distances (Newnham and de Haan, 1962), are missing from the EXAFS fit. Two factors may explain this discrepancy: first, the Cr has a local structure, out to only ≈ 4 Å, like that of Cr₂O₃ in the 1980s pit soil, and second, destructive interference of the EXAFS phase and amplitude parameters may be damping the EXAFS oscillations and their Fourier transform peaks. Both factors may be significant for this soil: first, microprobe analysis did not locate discrete Cr phases other than CaCrO₄, suggesting that the Cr(III) in the sample may be present as very small ($\ll 1 \mu\text{m}$) and dispersed particles of Cr₂O₃, and second, FEFF modeling of a Cr₂O₃ model compound, with reported 99.995% purity, also did not identify all of the theoretical Cr-Cr distances. The Cr-Cr distances that were found by EXAFS fitting of both the model compound and the 1980s pit soil agree to within 0.01–0.05 Å of XRD-determined Cr-Cr distances in Cr₂O₃. The presence of Cr₂O₃, rather than a Cr(III) oxyhydroxide precipitate phase, may be due to the composition of Cr waste introduced to this pit. Chromium plating usually requires the use of Cr₂O₃, combined with sulphuric acid (Greenwood and Earnshaw, 1984), and the waste mixture in this pit was partially from chromium plating operations at the national laboratory.

6.7.3. Sandia 1970s pit

The Sandia 1970s pit sample contains the highest amount of total Cr, 20,700 $\mu\text{g g}^{-1}$, only 2–7% of which is Cr(VI) (Table 2), and yet its EXAFS spectra are the noisiest of all

the natural soil samples examined. Low signal-to-noise in XAFS data typically signifies low concentration of the absorber element, a highly disordered local structure about the absorber element, or both. Clearly this soil sample is not low in Cr, so a possible conclusion is that the Cr is present in one or more poorly ordered phase(s). Well-crystallized grains of α -CrOOH (grimaldiite) were observed by TEM electron diffraction, however, and microprobe analysis showed $\geq 10 \mu\text{m}$ thick rims of CrOOH coating quartz and feldspar grains. FEFF fits to the 1970s pit soil EXAFS (Fig. 7d–f) identified Cr(VI)-O at 1.63 Å, Cr(III)-O at 1.95 Å, and Cr-Cr at 2.97 and 3.87 Å. The Cr(III)-O and Cr-Cr distances are consistent with the presence of Cr in a γ -CrOOH structure. A possible explanation to account for all of these observations is that the rim material is a mixture of crystalline and poorly crystalline CrOOH phases, combined with a small amount of a Cr(VI) phase. The low Cr(VI)/total Cr content in this sample precludes positive identification of the Cr(VI) phase by XAFS analysis. However, saturation index calculations for core material from this pit suggest that the most probable phase is a Cr(VI)-substituted gypsum, $\text{Ca}(\text{S,Cr})\text{O}_4 \cdot 2\text{H}_2\text{O}$ (Stein et al., 1994).

The magnetite fraction of the 1970s pit soil has less Cr present as Cr(VI), 2.2% as compared with 7.3% Cr(VI)/total Cr in the nonmagnetic fraction (Table 2), which is consistent with partial reduction of the Cr(VI) by electron transfer from Fe^{2+} in the magnetite structure. The Cr(VI)-O and Cr(III)-O distances determined from FEFF fits to the magnetite fraction EXAFS are similar to those determined from the nonmagnetic fraction EXAFS, but the Cr-Cr distances differ: Cr-Cr distances of 3.01 and 3.36 Å were derived from the EXAFS data from the magnetite fraction. These distances are consistent with a Cr(VI) phase, such as the $\text{Ca}(\text{S,Cr})\text{O}_4 \cdot 2\text{H}_2\text{O}$ predicted by saturation index calculations (Stein et al., 1994), and a Cr(III) phase such as α -CrOOH, which has Cr-Cr distances of 2.99 and 3.40 Å (Charlet and Manceau, 1992). The combined mineral fractions, therefore, contain mixtures of at least two Cr(III) oxyhydroxide phases. This finding is consistent with laboratory investigations (Charlet and Manceau, 1992) showing Cr(III) in a mixed α - and γ -(Cr,Fe)OOH local structure when adsorbed onto hydrous ferric oxide or goethite.

7. CONCLUSIONS AND IMPLICATIONS FOR SITE CHARACTERIZATION

EXAFS of Keyport samples, from a site contaminated by a single Cr point-source, reveal marked sample homogeneity (e.g., compare Fig. 6a, c, and e or Fig. 6b, d, and f), with the most prominent differences occurring not between soil samples, but between the magnetite and silicate mineral separates. The Keyport magnetite and silicate fractions have distinct XANES and EXAFS due to differences in the local environment around the Cr as a function of the mineral fraction, and different Cr(VI) contents due to Cr(VI)-to-Cr(III) reduction occurring at the magnetite surface. Analysis of Keyport samples demonstrates that XAFS spectroscopy may be used to characterize Cr phases formed by precipitation and sorption of Cr from waste solutions, as well as to identify Cr occurring naturally in minerals such as

magnetite and chromite. Chromium(VI)/total Cr contents were readily determined by calibrated pre-edge height measurements.

XAFS spectroscopy, combined with electron microprobe, TEM, and saturation index calculations of the various soils from waste disposal pits in use over three decades at Sandia National Laboratory show high variability of total Cr, Cr(VI)/Cr(III) ratios, and Cr phases present. A CrOOH precipitate is commonly present, along with Cr_2O_3 , CaCrO_4 , $\text{Ca}(\text{S,Cr})\text{O}_4 \cdot 2\text{H}_2\text{O}$, and CrPbO_4 , depending on the composition of the waste solution. Microprobe analysis proved valuable in corroborating the phase identification of those precipitates that are present as $>1 \mu\text{m}$ particles or grain-surface coatings.

Speciation and oxidation-state determination of Cr-contaminated soils may be readily accomplished by XAFS spectroscopic analysis. As illustrated in this paper, Cr phase identification by XAFS analysis reproduces quite well that done by electron microprobe analysis. Because XAFS analysis may be done in an ambient environment, with the sample in contact with water, metastable mineral phases that might decompose in ultra-high vacuum may also be identified by XAFS, as well as sorbate phases having only short-range order which would not be detected by electron microprobe or X-ray diffraction techniques. Sample preparation for XAFS analysis is minimal, eliminating the need for elaborate extraction, dissolution, or concentration techniques.

Segregation of the magnetic fraction of the soils resulted in the observation that Cr(VI) may be reduced in situ by reaction with magnetite. The quantity of magnetite typically present in soils, however, is too low for magnetite alone to be an effective agent of remediation. There is active interest in such in situ heterogeneous oxidation/reduction reactions, however, as demonstrated by the growing body of literature devoted to investigations of zero-valent Fe as an electron source for remediation of oxidized soil and ground water contaminants (e.g., Gillham and O'Hannesin, 1994; Cantrell et al., 1995; Wilson, 1995).

Acknowledgments—We are grateful to the National Science Foundation (grant #EAR-9406490) for financial support of this research, to the Corning Incorporated Foundation for a graduate student fellowship, to the Stanford Center for Materials Research for providing XPS and microprobe facilities, and to the staff of the Stanford Synchrotron Radiation Laboratory (particularly Britt Hedman) for their valuable assistance. SSRL is supported by the Department of Energy and the National Institutes of Health.

REFERENCES

- Anderson L. C. D., Kent D. A., and Davis J. A. (1992) Reduction of Cr(VI) under mildly reducing conditions in a sand and gravel aquifer. In *Water-Rock Interaction* (ed. Y. K. Kharaka and A. S. Maest), pp. 495–498. Balkema.
- Babich H. and Stotzky G. (1983) Influence of chemical speciation on the toxicity of heavy metals to the microbiota. In *Aquatic Toxicology* (ed. J. O. Nriagu), pp. 1–46. Wiley.
- Bajt S., Clark S. B., Sutton S. R., Rivers M. L., and Smith J. V. (1993) Synchrotron X-ray microprobe determination of chromate content using X-ray absorption near-edge structure. *Anal. Chem.* **65**, 1800–1804.
- Bidoglio G., Gibson P. N., O'Gorman M., and Roberts K. J. (1993) X-ray absorption spectroscopy investigation of surface redox

- transformations of thallium and chromium on colloidal mineral oxides. *Geochim. Cosmochim. Acta* **57**, 2389–2394.
- Briggs D. and Seah M. P., ed. (1990) *Practical Surface Analysis*. 2nd ed. Wiley.
- Brown G. E., Jr., Calas G., Waychunas G. A., and Petiau J. (1988) X-ray absorption spectroscopy and its applications in mineralogy and geochemistry. In *Spectroscopic Methods in Mineralogy* (ed. F. C. Hawthorne); *Rev. Mineral. MSA*, **18**, pp. 431–512.
- Burns R. G. (1993) *Mineralogical Applications of Crystal Field Theory*, 2nd ed. Cambridge Univ. Press.
- Cantrell K. J., Kaplan D. I., and Wietsma T. W. (1995) Zero-valent iron for the in situ remediation of selected metals in ground water. *J. Haz. Materials* **42**, 201–212.
- Charlet L. and Manceau A. (1992) X-ray absorption spectroscopic study of the sorption of Cr(III) at the oxide-water interface. *J. Colloid Interface Sci.* **148**, 443–458.
- Corker J. M., Evans J., and Rummey J. M. (1991) XAFS studies of pillared clay catalysts. *Materials Chem. Phys.* **29**, 201–209.
- Eary L. E. and Rai D. (1988) Chromate removal from aqueous waste by reduction with ferrous ion. *Environ. Sci. Tech.* **22**, 972–977.
- Eary L. E. and Rai D. (1991) Chromate reduction by subsurface soils under acidic conditions. *Soil Sci. Soc. Amer. J.* **55**, 676–683.
- Farges F., Brown G. E., Jr., and Rehr J. J. (1996) Coordination chemistry of Ti(IV) in silicate glasses and melts. 1. XAFS study of Ti coordination in oxide model compounds. *Geochim. Cosmochim. Acta* **60**, 3023–3053.
- Fendorf S. E. and Guangchao L. (1996) Kinetics of chromate reduction by ferrous iron. *Environ. Sci. Tech.* **30**, 1614–1617.
- Fendorf S. E., Lamble G. M., Stapleton M. G., Kelley M. J., and Sparks D. L. (1994) Mechanisms of chromium(III) sorption on silica. 1. Cr(III) surface structure derived by extended X-ray absorption fine structure spectroscopy. *Environ. Sci. Tech.* **28**, 284–289.
- George G. N. (1995) EXAFSPAK: A Suite of Computer Programs for Analysis of X-ray Absorption Spectra. Stanford Synchrotron Radiation Lab.
- Gillham R. W. and O'Hannesin S. (1994) Enhanced degradation of halogenated aliphatics by zero-valent iron. *Ground Water* **32**, 958–967.
- Greenwood N. N. and Earnshaw A. (1984) *Chemistry of the Elements*. Pergamon.
- Ilton E. S. and Veblen D. R. (1994) Chromium sorption by phlogopite and biotite in acidic solutions at 25°C: Insights from X-ray photoelectron spectroscopy and electron microscopy. *Geochim. Cosmochim. Acta* **58**, 2777–2788.
- Kent D. B., Davis J. A., Anderson L. C. D., Rea B. A., and Waite T. D. (1994) Transport of chromium and selenium in the suboxic zone of a shallow aquifer: Influence of redox and adsorption reactions. *Water Resour. Res.* **30**, 1099–1114.
- Lewis R. J., Sr., ed. (1991) *Carcinogenically Active Chemicals*. Van Nostrand Reinhold.
- Lytle F. W. (1989) Experimental X-ray absorption spectroscopy. In *Applications of Synchrotron Radiation* (ed. H. Winick), pp. 135–223. Gordon and Breach.
- Lytle F. W. et al. (1984) Measurement of soft X-ray absorption spectra with a fluorescent ion chamber detector. *Nucl. Instrum. Methods* **226**, 542–548.
- Newnham R. E. and de Haan Y. M. (1962) Refinement of the α Al_2O_3 , Ti_2O_3 , V_2O_3 , and Cr_2O_3 structures. *Z. Kristallogr.* **117**, 235–237.
- O'Neill P. (1985) *Environmental Chemistry*. Unwin Hyman.
- Peterson M. L., Brown G. E., Jr., and Parks G. A. (1996a) Direct XAFS evidence for heterogeneous redox reaction at the aqueous chromium/magnetite interface. *Colloids Surfaces A* **107**, 77–88.
- Peterson M. L., Brown G. E., Jr., and Parks G. A. (1996b) Quantitative determination of chromium valence in environmental samples using XAFS spectroscopy. *Proc. Mater. Res. Soc. Spring Mtg. San Francisco* **432**, 75–80.
- Peterson M. L., White A. F., Brown G. E., Jr., and Parks G. E. (1997) Surface passivation of magnetite (Fe_3O_4) by reaction with aqueous Cr(VI): XAFS and TEM results. *Environ. Sci. Tech.* **31**, 1573–1576.
- Public Health Service Drinking Water Standards (1962) U.S. Dept. of Health, Education, and Welfare, U.S. Government Printing Office: Washington DC.
- Ravel B. (1995) *ATOMS v. 2.42d*. Univ. of Washington.
- Snow E. T. and Xu L. S. (1989) Effects of chromium-III on DNA replication in vitro. *Biol. Trace Element Res.* **21**, 61–72.
- Stein C. L., Amonette J. E., Olivier J. A., and Huang D. L. (1994) Geochemistry of anthropogenic chromium in calcareous sediments. Poster presentation at the Soil Sci. Soc. America Annual Meeting, Seattle, WA, Nov. 1994.
- Tessier A., Campbell P., and Bisson M. (1979) Sequential extraction procedure for the speciation of particulate trace metals. *Anal. Chem.* **51**, 844.
- White A. F. and Peterson M. L. (1996) Reduction of aqueous transition metal species on the surfaces of Fe(II)-containing oxides. *Geochim. Cosmochim. Acta* **60**, 3799–3814.
- Wilson E. K. (1995) Zero-valent metals provide possible solution to ground water problems. *Chem. Eng. News* **73**, 19–23.
- Zabinsky S. I., Rehr J. J., Ankudinov A., Albers R. C., and Eller M. J. (1995) Multiple-scattering calculations of X-ray-absorption spectra. *Phys. Rev. B* **52**, 2995–3009.